CHEMISTRY OF MATERIALS

pubs.acs.org/cm

Article

Influence of Ge Lone Pairs on the Elasticity and Thermal Conductivity of GeSe–$AgBiSe_2$ Alloys

Mario Calderón-Cueva, Eleonora Isotta, Megan Rylko, Binayak Mukherjee, Paolo Scardi, and Alexandra Zevalkink*

Cite This: https://doi.org/10.1021/acs.chemmater.3c01616

Read Online

ACCESS | Metrics & More | Article Recommendations | Supporting Information

ABSTRACT: Chemical design is a compelling strategy to improve the performance of energy materials but requires a comprehensive understanding of how structure and chemistry affect materials properties. In this work, we investigate the structural, elastic, and thermal behavior of the $(GeSe)_{1-x}$–$(AgBiSe_2)_x$ system to shed light on the respective contributions of chemistry and crystal structure to thermal transport. In this system, progressive $AgBiSe_2$ alloying transforms the room-temperature structure from orthorhombic to rhombohedral to cubic rock-salt, with the latter being the thermodynamically stable phase across the entire compositional range at a high temperature. Within a given structure type, alloying progressively increases point-defect phonon scattering and decreases the speed of sound, thus reducing the lattice thermal conductivity. However, an anomalous increase in thermal conductivity is noticed upon the transition from the rhombohedral to the cubic phase, associated with a large step-like increase in the elastic moduli. Density functional theory calculations suggest this change in stiffness is due to the tendency of Ge to exhibit strongly expressed lone-pair orbitals. The lone pairs switch from fully oriented in the rhombohedral phase to randomly oriented in the cubic phase, leading to an overall bond stiffening. Supporting this argument, increased $AgBiSe_2$ content, and thus weakened lone-pair expression, leads to a less pronounced stiffening at the phase transition. These findings help improve our understanding of the intrinsic properties of this system and the design of rock-salt chalcogenides with tailored thermal properties.

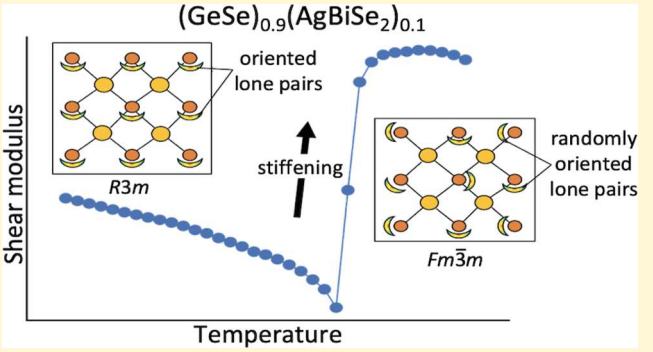

INTRODUCTION

One potential route to counter the environmental impact of ever-increasing worldwide energy consumption is to recover energy from waste heat using thermoelectric (TE) devices. A material's thermal-to-electric energy conversion efficiency is measured through the dimensionless TE figure of merit $zT = S^2\sigma T\kappa^{-1}$, with S, σ, κ, and T being the Seebeck coefficient, electrical conductivity, thermal conductivity, and absolute temperature, respectively. κ can be expressed as the sum of the lattice, κ_L, and the electronic, κ_e, thermal conductivity, $\kappa = \kappa_L + \kappa_e$. From these two equations, it becomes evident that the suppression of κ is needed to maximize zT, although without detrimental effects on the electronic properties. For this reason, it is imperative to study the heat transport from the collective lattice vibrations (phonons) and isolate the effect of lattice dynamics on κ_L. It is well known[1,2] that the frequency-dependence of heat-carrying phonons can be exploited to achieve a low κ by means of phonon scattering by defect[3−6] and micro- and nanostructural manipulation[7−9] of the material. However, the intrinsic role of composition and crystal structure on κ_L is more elusive.[10,11] Understanding the fundamental connections between chemistry, structure, and transport properties represents a powerful tool toward the chemical design of high-preforming TEs. For this purpose, the present study focuses on the relation between the structure, composition and their effect on the intrinsic low lattice thermal conductivity in the $(GeSe)_{1-x}$–$(AgBiSe_2)_x$ system.

Chalcogenide-based IV–VI compounds, particularly cubic PbTe,[12−15] rhombohedral GeTe,[16−19] and orthorhombic SnSe,[20,21] show excellent TE efficiency ($zT \sim 2$) in the mid-temperature range (550–800 K). For instance, polycrystalline SnSe achieved an average TE figure of merit zT of 2 in the temperature range 400–783 K.[22] Although recent theoretical studies proposed orthorhombic GeSe as a highly efficient ($zT > 2$) n-type material upon carrier-density optimization,[23] several experimental results show a p-type behavior and a low zT (<0.2).[24,25] The need to improve the TE performance of

Received: June 28, 2023
Revised: October 1, 2023

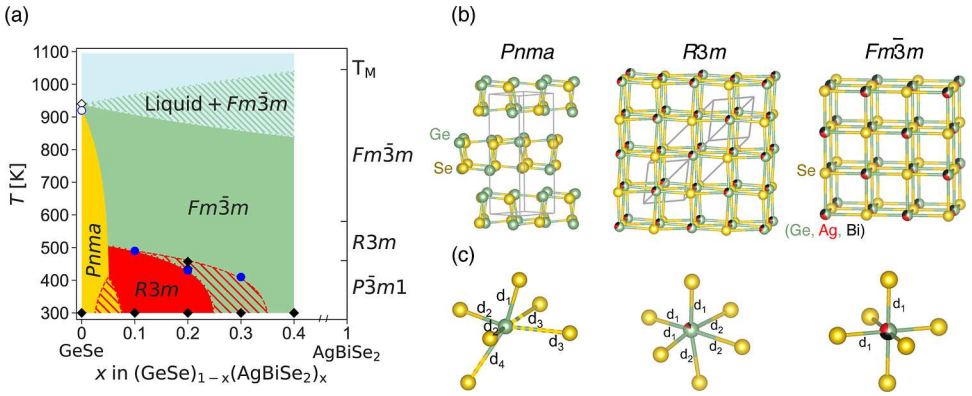

Figure 1. (a) Phase diagram for the $(GeSe)_{1-x}-(AgBiSe_2)_x$ system from $x = 0$ to $x = 0.4$. Black ◆ and blue ● data points correspond to XRD and DSC experiments, respectively, performed in this work; ◇ and blue ○ are experimental XRD and DSC values, respectively, from ref 34. (b) Three ambient-temperature structures from $x = 0$ to $x = 0.4$: orthorhombic *Pnma*, rhombohedral *R*3*m*, and cubic *Fm*$\bar{3}$*m*. (c) Coordination environment and unique bonds for the respective cation coordination environments in (b).

GeSe has led researchers to try different dopants, such as Na[26] and Ag/Bi/Pb,[24] and alloying with $AgSbTe_2$. More recently, GeSe was alloyed with $AgBiSe_2$[25]—trigonal *P*$\bar{3}$*m*1 at ambient temperature[27]—successfully obtaining n-type conduction above 40% of alloying. Interestingly, the authors found that the system crystallizes in three different structures, orthorhombic, rhombohedral, and cubic, within an alloying range of 0−40% of $AgBiSe_2$ (Figure 1). Namely, GeSe crystallizes in the orthorhombic structure (*Pnma*), while above 10% of $AgBiSe_2$ alloying, the unit cell is rhombohedral (*R*3*m*) and becomes cubic (*Fm*$\bar{3}$*m*) above 40% alloying. The formation of the cubic structure appears to be driven by entropy since the orthorhombic and rhombohedral arrangements eventually transform into the cubic one at a high temperature. A crucial result of that study, and a more recent one,[28] was the observation of ultralow κ_L for the $(GeSe)_{1-x}-(AgBiSe_2)_x$ system, especially in alloys with rhombohedral symmetry.

Because the $(GeSe)_{1-x}-(AgBiSe_2)_x$ system exhibits three important crystal structures, it provides a platform for understanding and decoupling the effect of the composition and crystal structure on κ_L. Notable prior investigations across various material families[29−33] have discussed the importance of Ge lone pairs in heat transport. Nevertheless, these earlier studies have predominantly overlooked a crucial aspect: the substantial stiffening that accompanies the martensitic rhombohedral-to-cubic phase transition. Here, we quantify this stiffening and explore its effects on the thermal conductivity of the $(GeSe)_{1-x}-(AgBiSe_2)_x$ system using a combination of high-temperature resonant ultrasound spectroscopy (RUS), high-temperature X-ray diffraction (HT-XRD), transport measurements, and density functional theory (DFT) calculations, to reveal the fine relationship connecting the crystal structure and composition to the speed of sound, phonon scattering, and ultimately κ_L. These results contribute to the understanding of the parameters that govern each aspect of the lattice thermal conductivity and can guide the chemical design of high-performing TE materials with ultralow κ_L.

METHODS

Sample Synthesis. Stoichiometric amounts of Ag, Bi, Ge, and Se were weighted in an Ar-filled glovebox (O_2 and H_2O < 1 ppm) to obtain the five compositions of $(GeSe)_{1-x}-(AgBiSe_2)_x$ with $x = 0$, 0.1, 0.2, 0.3, and 0.4. These were sealed in quartz ampules under running vacuum (~10^{-4} Torr) and heated in a box furnace from ambient temperature to 673 K over 12 h. The ampules were soaked at the said temperature for 4 h, then brought to 1173 K in 7 h, and kept for 10 h. Finally, they were cooled to room temperature in 18 h. The obtained ingots were crushed in a glovebox using a mortar and pestle. For each composition, approximately 5 g of powder was loaded into cylindrical graphite dies of 10 mm inner diameter and consolidated into solid pucks via the spark plasma sintering (SPS) technique, using a Dr. Sinter LAB 211Lx (Fuji Electronic Industrial Co.) under vacuum. For all compositions, the same SPS pressure (50 MPa) and temperature profile was used: heating to 773 K in 24 min, held at that temperature for 20 min, after which the pressure was decreased to 3 MPa. Then, the sample was allowed to cool to room temperature inside the SPS in 25 min. The obtained SPS samples were 10 mm in diameter and 3−5 mm in height. These profiles were determined after several unsuccessful attempts, which either did not yield the desired phases or resulted in cracked SPSed pucks. Reducing the pressure during cooling was necessary to avoid cracking of the samples. The SPSing temperature for all alloys was estimated as 80% of the melting temperature of GeSe, as reported in ref 25.

Structural Characterization. The phase purity of the crushed ingots and of the SPS samples was checked with room temperature XRD, using a Rigaku SmartLab instrument, with a Cu Kα radiation source (λ = 1.5406 Å). A Rietveld refinement of XRD data was performed with the GSAS-II software for crystallographic information and with the TOPAS 6 Academic[35] software for microstructural details.[36,37] For HT-XRD experiments, pristine samples, that is, samples that were not previously used for any experiment, of $(GeSe)_{1-x}-(AgBiSe_2)_x$ with $x = 0.2$ and 0.4, were crushed into fine powders using a mortar and pestle and then loaded onto a Rigaku HT1500 high-temperature stage. XRD patterns were collected in the range of 300−600 K during the heating cycle. A rate of 10 K/min was used, allowing the sample temperature to stabilize before each collection for 6 min, during which time a height alignment was performed. For the heating cycle, diffraction patterns were collected every 20 K from 303 to 423 K, every 10 K from 423 to 503 K, and again every 20 K from 503 to 603 K. These steps were chosen to intensify the collection during the phase transition.

Thermal Analyses. Differential scanning calorimetry (DSC) and thermogravimetric analysis (TGA) were performed with a NETZSCH STA 449C apparatus. Around 10 mg of the samples in the form of fine powders were loaded in Al crucibles and measured in the temperature range of 300−673 K, with a ramp of 5 K/min and under a 20 mL/min flow of Ar. The measurement was repeated twice to see the reversibility of processes. The complete data can be found in Supporting Information Figure S2.

Resonant Ultrasound Spectroscopy. The temperature-dependent elastic moduli and speed of sound were obtained via RUS, performed with ambient- and high-temperature stages (Alamo Creek Engineering, New Mexico, USA). Samples were polished to obtain cylinders of 10 mm diameter and approximately 3 mm in height and

https://doi.org/10.1021/acs.chemmater.3c01616
Chem. Mater. XXXX, XXX, XXX−XXX

balanced between two transducers inside a furnace under flowing Ar. RUS spectra were recorded from 300 to 673 K in intervals of 10 K and with a frequency range of 50−400 kHz. Sufficient time was allowed between temperature steps for the sample to thermally stabilize. The RUS patterns were acquired via the open-source, LabVIEW ResonanceSpectrometer Software.[38] Subsequently, the resonant peak positions were determined within the same software using a Lorentzian fit. Finally, the elastic moduli were determined by fitting the experimental data in the Cyl.exe program.[39]

Thermal and Electronic Properties. The total thermal conductivity (κ) was calculated as $\kappa = C_P \rho D$, where C_P, ρ, and D are the specific heat capacity at constant pressure, the geometric density, and the thermal diffusivity, respectively. For thermal diffusivity experiments, the SPS pellets were cut into approximately 1 mm thick disks. D was recorded in heating and cooling every 10 K in a temperature interval of 300−673 K using a laser flash apparatus (NETZSCH LFA 467). The C_P is treated as temperature-independent and calculated using the Dulong−Petit approximation. The obtained values for C_P and ρ are summarized in Table 1, along with the theoretical density (ρ_T from XRD). The Seebeck coefficient was measured in a uniaxial four-probe arrangement using the slope method,[40] with 60 min sinusoidal temperature oscillations with a maximum temperature difference of 5 K. Measurements were performed in the temperature range of 323−548 K, with a step of 50 K and a heating rate of 120 K/min. The electrical resistivity was measured in the van der Pauw configuration in the temperature range of 303−673 K, with a heating rate of 1.5 K/min and a current of 100 mA.

Table 1. Dulong−Petit Heat Capacity (C_P), Geometric Density (ρ), Theoretical Density (ρ_T), and Relative Density (ρ/ρ_T)[a]

composition $(GeSe)_{1-x}-(AgBiSe_2)_x$	C_P [J/g K]	ρ [g/cm^3]	ρ_T [g/cm^3]	ρ/ρ_T
$x = 0$	0.330	5.53	5.53	1.00
$x = 0.1$	0.310	5.76	5.90	0.98
$x = 0.2$	0.295	5.98	5.98	1.00
$x = 0.3$	0.285	6.19	6.31	0.98
$x = 0.4$	0.277	6.46	6.87	0.94

[a]For the synthesized samples in the $(GeSe)_{1-x}-(AgBiSe_2)_x$ system.

Density Functional Theory. The DFT calculations have been performed with the Vienna Ab initio Simulation Package (VASP).[41,42] The disordered, alloyed cubic ($Fm\bar{3}m$) and rhombohedral ($R3m$) structures are represented by 64-atom and 72-atom supercells, respectively. The disordered structures were generated by randomly assigning Ge, Ag, and Bi to the cation sites. The computations have been performed using the Perdew−Burke−Ernzerhof form of the generalized gradient approximation to the electron exchange−correlation functional,[43] specifically within the PBEsol implementation, which improves the equilibrium properties of the solids.[44] A plane-wave basis set expanded up to a cutoff energy of 450 eV, and a 2 × 2 × 1 Monkhorst−Pack Γ-centered k-mesh is used to sample the irreducible Brillouin zone. A Gaussian charge smearing of 0.01 eV is applied, and the Hellman−Feynman forces on individual ions are converged to below 0.01 eV/Å, with electronic degrees of freedom minimized until the change in energy is below 10^{-6} eV. The charge densities and electron localization function (ELF) maps are visualized using VESTA.[45]

RESULTS AND DISCUSSION

Crystal Structure Evolution as a Function of Composition. The XRD experiments on the $(GeSe)_{1-x}-(AgBiSe_2)_x$ samples from this study (Figure 2) confirmed the reported literature phases.[25] Crystallographic and microstructural parameters from a Rietveld refinement of XRD data can be found in Supporting Information Tables S1 and S2. The $x = 0$ sample displays an orthorhombic structure (space group *Pnma*, Figure 1b), as extensively reported for pure GeSe.[46−49] The literature data at 10% ($x = 0.1$)[28] and 20% ($x = 0.2$)[50] alloying was also confirmed, showing instead a rhombohedral $R3m$ phase (Figure 1b). The other end member of the present research, that is at 40% alloying, displays a rock-salt cubic structure (space group $Fm\bar{3}m$, Figure 1b), as described previously.[25] Interestingly, the Rietveld refinement for the $x = 0.3$ sample points to a coexistence of the $R3m$ and $Fm\bar{3}m$ phases. This can indicate that the composition is in a two-phase region. The increase in alloying within the rhombohedral system (see Supporting Information Table S1) is accompanied by a slight increase in lattice parameters as the larger Ag and Bi substitute for Ge on the cation site.

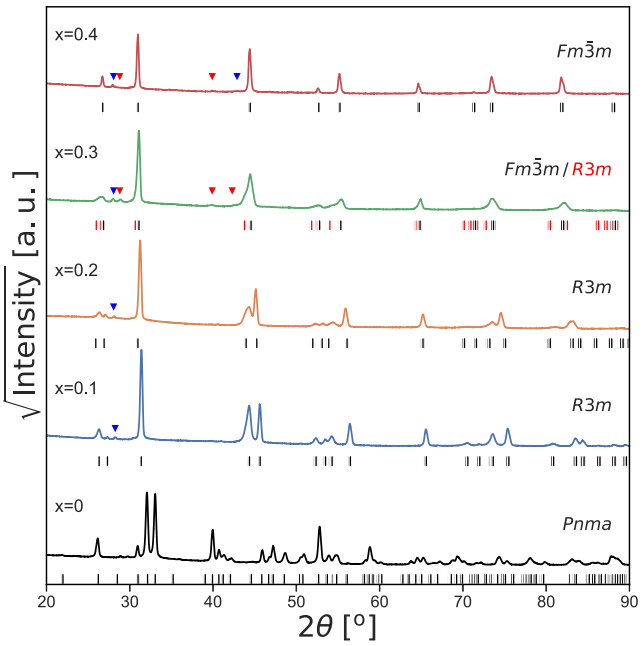

Figure 2. XRD patterns of the $(GeSe)_{1-x}-(AgBiSe_2)_x$ system at room temperature. With the progressive incorporation of $AgBiSe_2$, the structure evolves from orthorhombic *Pnma* ($x = 0$) to rhombohedral $R3m$ ($x = 0.1-0.3$) and finally to the high-symmetry rock-salt cubic $Fm\bar{3}m$ ($x = 0.3-0.4$). Blue ▼ and red ▼ denote the presence of minor impurity phases Bi_4Se_3 and Ag_8GeSe_6, respectively. The square root of the XRD intensity is plotted to highlight any peaks from the secondary phases. XRD was performed on SPSsed samples.

The observed evolution toward higher-symmetry structural arrangements with the incorporation of $AgBiSe_2$ has been attributed to the increase in entropy associated with alloying.[25] The orthorhombic structure of GeSe can be considered to consist of highly distorted octahedra of Ge atoms coordinated by six Se atoms. Such an environment, as shown in Figure 1c, displays four different bond lengths. This configuration becomes a less distorted octahedron in the rhombohedral phase, where only two distinct bonds are present. These eventually evolve into one unique bond length for cubic symmetry. Coherently, with increasing temperature, all the compositions are reported to eventually transition to a $Fm\bar{3}m$ cubic structure, as happens for both the end members of GeSe[34,50] and $AgBiSe_2$.[51]

With the aid of DSC (Supporting Information Figure S2) and HT-XRD, the phase-transition temperature for compositions $x = 0.1$, $x = 0.2$, and $x = 0.3$ was determined. This depends on the alloying fraction. The results are arranged in

https://doi.org/10.1021/acs.chemmater.3c01616
Chem. Mater. XXXX, XXX, XXX−XXX

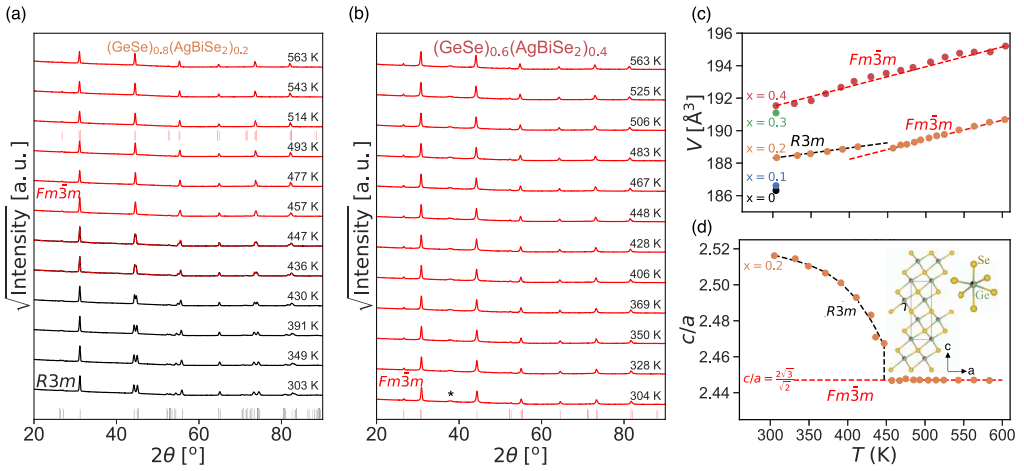

Figure 3. High-temperature XRD patterns for (a) $(GeSe)_{0.8}$−$(AgBiSe_2)_{0.2}$ and (b) $(GeSe)_{0.6}$−$(AgBiSe_2)_{0.4}$. Note the phase transition for the x = 0.2 sample from a rhombohedral (in black) to a cubic (red) arrangement above 457 K. The peak at 2θ = 38° in panel b (denoted by *) corresponds to contaminants on the HT-stage window. (c) Unit cell volume vs temperature for all the compositions, with high-temperature data for the x = 0.2 and x = 0.4 samples and ambient-temperature data for the others. The unit cell volume increases for increasing alloying, as expected considering the larger ionic radii of Ag and Bi with respect to Ge. (d) Lattice parameter ratio evolution with temperature for the $(GeSe)_{0.8}$−$(AgBiSe_2)_{0.2}$ sample.

the phase diagram reported in Figure 1a, where the symbols black ◆ and blue ● depict XRD and DSC values, respectively. The reported literature value of 925 K for the phase transition of GeSe from orthorhombic to cubic is included (○ symbol),[34] whereas the liquidus line was estimated from the reported melting temperature of the GeSe (blue ◇) and $AgBiSe_2$ (T_M) end members, as reported in refs 34 and 52, respectively. The $AgBiSe_2$ phase transformation temperatures were taken from ref 27.

Crystal Structure Evolution as a Function of Temperature. HT-XRD patterns were collected on the x = 0.2 and x = 0.4 samples of the $(GeSe)_{1-x}$−$(AgBiSe_2)_x$ system. The results are summarized in Figure 3, while the full data from the Rietveld refinements can be found in the Supporting Information.

The x = 0.2 sample revealed a phase transition from the rhombohedral to the cubic structure at approximately 457 K (Figure 3a), which is consistent with the reported literature value.[25] This is clearly noticeable in the peaks around 2θ = 45°, characteristic of the $R3m$ phase, that merge into a unique one above 450 K. For the x = 0.4 sample, as shown in Figure 3b, no phase transition is noticed up to 563 K. To allow a comparison of the lattice parameters, the cubic cell was converted to the equivalent rhombohedral (hexagonal setting) one according to the method in the Supporting Information. The rhombohedral phase in the x = 0.2 sample shows a shallower temperature slope than the cubic phase for both the x = 0.2 and x = 0.4 compositions. Using linear regressions, the coefficients of volumetric thermal expansion (α_V) of the x = 0.2 sample were calculated to be 3.28 × 10^{-5} and 5.72 × 10^{-5} °C^{-1} for the rhombohedral and cubic phases, respectively, and 6.73 × 10^{-5} °C^{-1} for the x = 0.4 sample. Figure 3d shows the temperature dependence of the c/a lattice parameter ratio for x = 0.2. When $c/a = 2\sqrt{3/2}$, the cubic symmetry forms. The larger volume of the rhombohedral with respect to the cubic unit cell is evidenced by two aspects. The first is the volume contraction after the phase transition in the x = 0.2 sample; a similar behavior has been observed in other compounds featuring analogous cubic-to-rhombohedral phase transitions, for instance, SnTe,[53] GeTe,[54] and SnTe−GeTe alloys,[55] among others.[56] The second aspect lies in the room-temperature unit cell volume of the alloyed compositions (Figure 3c). Indeed, while this is found to progressively increase as a function of alloying, the x = 0.4 sample appears to defy the otherwise linear trend. The trend of bond lengths is presented in Table 2,

Table 2. Bond Lengths at Room Temperature in the $(GeSe)_{1-x}$−$(AgBiSe_2)_x$ System Were Obtained from Rietveld Refinements of XRD Data

composition	d_1 (Å)	d_2 (Å)	d_3/d_4 (Å)	d_{avg} (Å)
x = 0 ($Pnma$)	2.54	2.56	3.30/3.41	2.95
x = 0.1 ($R3m$)	2.69	3.02	n/a	2.86
x = 0.2 ($R3m$)	2.71	3.03	n/a	2.87
x = 0.3 ($R3m$) 60% weight	2.72	3.04	n/a	2.88
x = 0.3 ($R3m$) 40% weight	2.88	n/a	n/a	2.88
x = 0.4 ($Fm\bar{3}m$)	2.88	n/a	n/a	2.88

including the average bond length for each composition (d_{avg}) calculated using the Ge/Bi/Ag−Se coordination of nearest neighbors depicted in Figure 1c. Interestingly, d_{avg} shrinks from x = 0 to x = 0.1, while there is a progressive increase of the average bond length with increasing alloying.

Elasticity and Bonding Evolution. *High-Temperature Elastic Moduli and Speed of Sound.* High-temperature RUS measurements were performed on the GeSe−$AgBiSe_2$ alloys to determine how changes in structure and bonding affect the elastic moduli and, in turn, the speed of sound and thermal conductivity. The polycrystalline samples were assumed to be elastically isotropic. Here, we report the obtained shear (G), bulk (B) and Young's (Y) moduli, and the Poisson ratio (μ), as well as the longitudinal (v_l) and transverse (v_t) speeds of sound, which were calculated as $v_l = \left[\left(B + \frac{4}{3}G\right)/\rho\right]^{1/2}$ and $v_t = [G/\rho]^{1/2}$, where ρ is the density. The average speed of sound (v_s) is estimated with

$$v_s = \left(\frac{1}{3}\left[\frac{1}{v_l^3} + \frac{2}{v_t^3}\right]\right)^{-1/3} \quad (1)$$

https://doi.org/10.1021/acs.chemmater.3c01616
Chem. Mater. XXXX, XXX, XXX−XXX

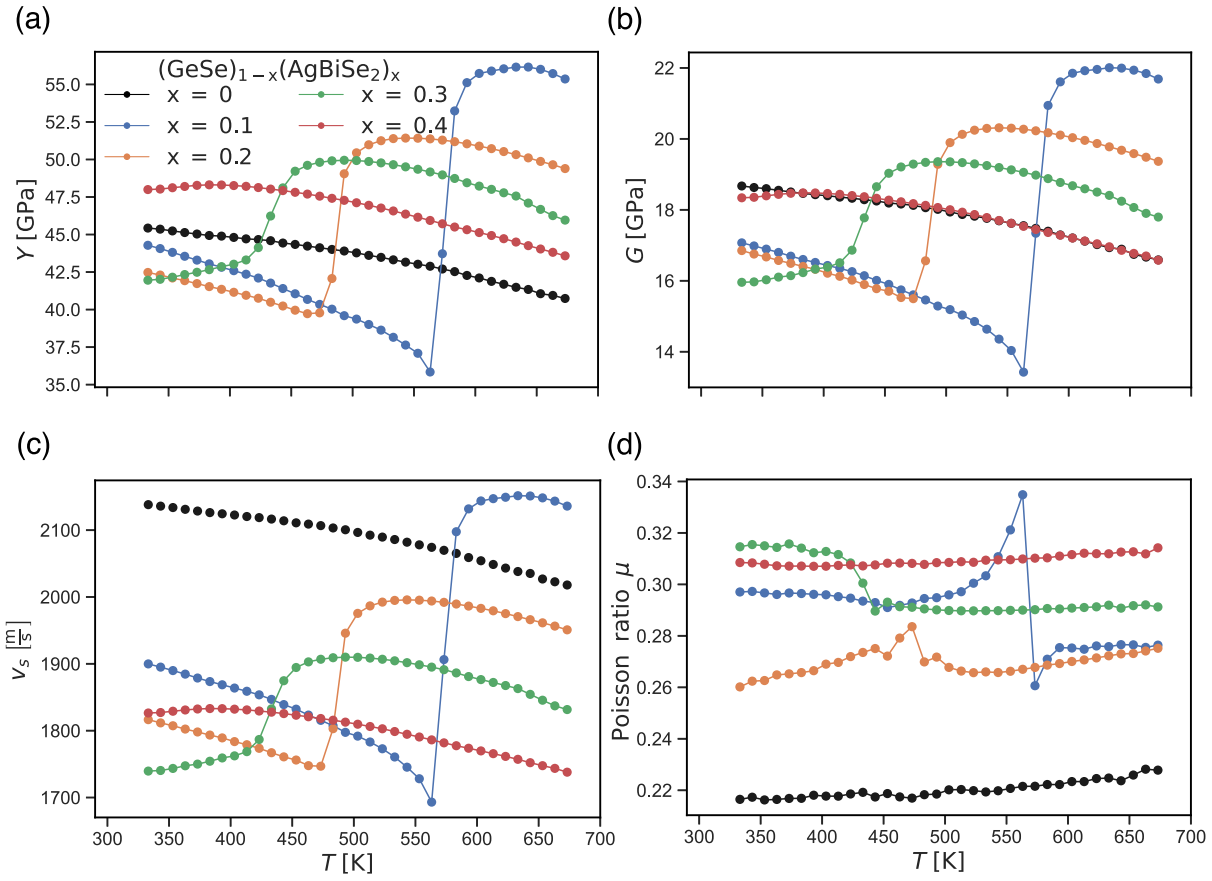

Figure 4. Temperature dependence of (a) Young's modulus, Y, (b) shear modulus, G, (c) speed of sound, v_s, and (d) Poisson's ratio, μ. For the x = 0.1, x = 0.2, and x = 0.3 compositions, the phase transition to the cubic structure leads to a dramatic stiffening. Instead, a substantial softening with increasing Ag/Bi substitution can be noticed when comparing samples in the same structural arrangement (x = 0.1, 0.2, and 0.3 before the phase transition and x = 0.1, 0.2, 0.3, and 0.4 above the phase transition).

The resulting temperature-dependent values of G, Y, v_s, and μ are shown in Figure 4, while B, v_t, and v_l are shown in Supporting Information Figure S5.

The observed trends in the elastic moduli (Figure 4a,b) are complex but can help explain some of the trends in κ_L. The first notable trend is that, as one should expect, within the same crystal structure, replacing Ge by the larger Ag and Bi cations leads to a softening (decrease) of the elastic moduli and a decrease in the sound velocity. This trend is especially apparent at a high temperature, when x = 0.1 through x = 0.4 compositions are in the cubic phase. The second, more surprising, feature of this data set is that the phase transition from the rhombohedral to the cubic arrangement leads to a very large increase in both the elastic moduli and speed of sound. This step-like stiffening is most pronounced for the x = 0.1 composition, which stiffens by ~53% at the phase transition. The effect lessens as x increases (only an ~ 16% stiffening of the x = 0.3 composition). It is also notable that, at room temperature, the x = 0.4 sample is stiffer than any other sample, despite the larger unit cell and longer bonds. We can therefore conclude that the transition to the high-symmetry cubic phase causes a significant stiffening of the structure. It is worth mentioning that the shear moduli G (Figure 4b) of the two end-compositions, that is, GeSe and $(GeSe)_{0.6}$–$(AgBiSe_2)_{0.4}$ are very similar. The explanation for such behavior requires us to consider two different variables: first, the increase in the Ag/Bi content tends to decrease the elastic moduli, and second, the change from the orthorhombic to the cubic crystal structure drastically increases the elastic moduli. The origin of this stiffening and the correlation between the degree of stiffening and composition are explored below.

Atomistic Perspective on the Nature of Bonding. To help explain the change in stiffness for the $(GeSe)_{1-x}$–$(AgBiSe_2)_x$ system across different structures and compositions, DFT calculations were first carried out for two disordered supercells: one with a composition of x = 0.2 with a $R3m$ unit cell and one with x = 0.4 and $Fm\bar{3}m$ symmetry. The ELF isosurfaces and sections are shown in Figure 5a,b,d,e for both supercells.

In both structures, a strong localization of electrons around the Se ions attests to a significant ionic character of bonds. However, some localization around Ge and Bi, as well as in the space between the cations and Se, points to a covalent contribution to the Ge–Se and Bi–Se bonds.[57] The latter is further confirmed by a finite overlap of electron densities between Se and the Ge and Bi cations, as observed in the charge density maps in Figure S6a,b, Supporting Information. This mixed ionic–covalent bonding is in sharp contrast to the Ag–Se bond, which is purely ionic in nature, as evidenced by the complete delocalization of electrons in the region surrounding Ag (Figure 5b,e), and a corresponding absence of charge density overlapping between the Ag and Se ions (in Figure S6, Supporting Information). This variation in bonding can be explained by considering the electronic configurations of the cations: both Bi ($6s^2$ $6p^3$) and Ge ($4s^2$ $4p^2$) have p-orbitals in their valence shell, promoting the formation of covalent bonds; Ag ($4d^{10}$ $5s^1$) has instead a single s electron,

https://doi.org/10.1021/acs.chemmater.3c01616
Chem. Mater. XXXX, XXX, XXX–XXX

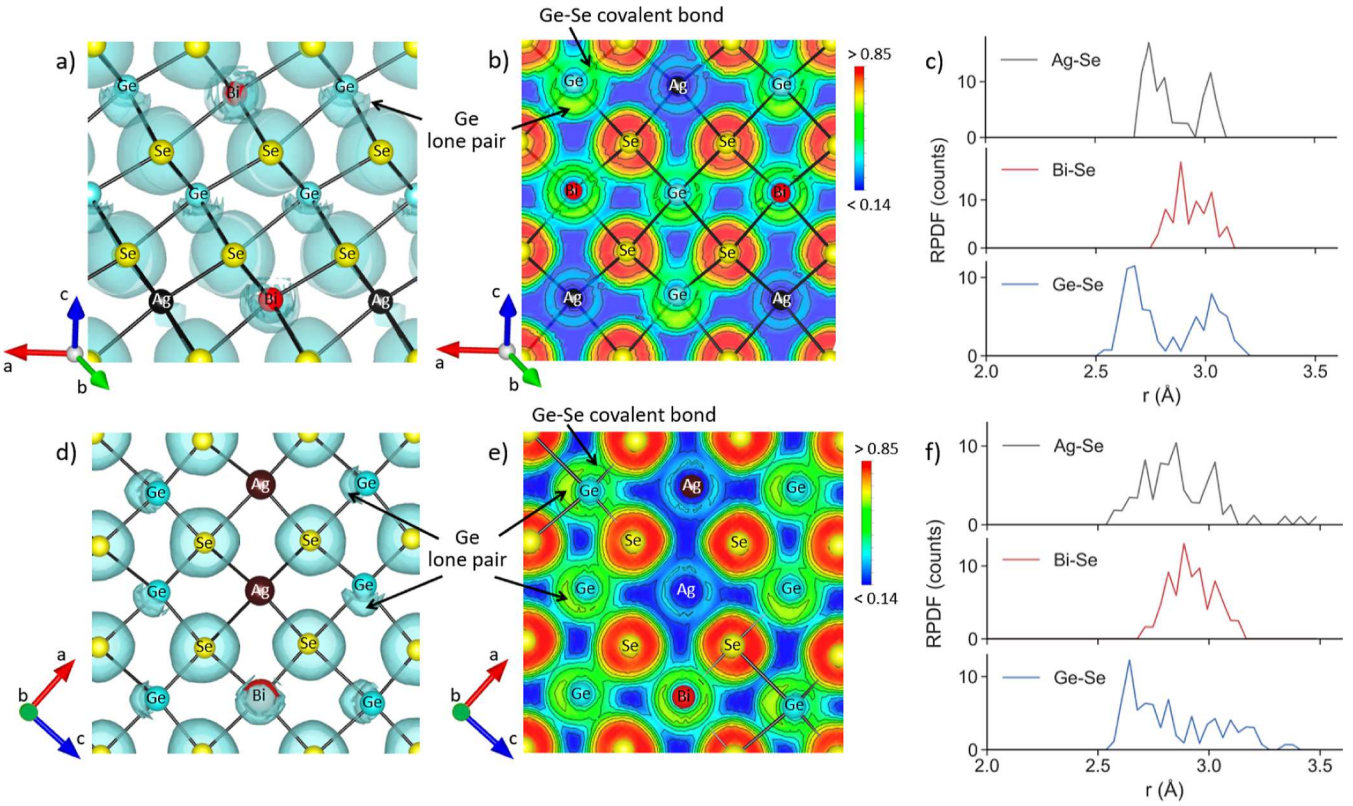

Figure 5. ELF isosurfaces (a,d) and sections (b,e), as well as radial pair distribution function (c,f) for the $R3m$ structure of $(GeSe)_{0.8}(AgBiSe_2)_{0.2}$ (a−c) and the $Fm\bar{3}m$ structure of $(GeSe)_{0.6}(AgBiSe_2)_{0.4}$ (d−f). The figures illustrate the polar-covalent bonding of Ge and Bi with Se, in contrast to the more ionic nature of the Ag−Se bond. The bimodality of the Ge−Se bond shown in panel c is attributed to the stereochemical expression of the Ge lone-pairs, which in the $R3m$ structure are all aligned along the same direction (see panels a,b), causing the structure to expand, in contrast to the random orientation that they show in the cubic arrangement (see panels d,e). This is believed to be at the origin of the elastic stiffening happening with the transition from rhombohedral to cubic.

which is easily delocalized, leading to the formation of a purely ionic bond. This is further supported by the difference of Pauling electronegativities between Se (2.55) and Ag (1.93), much greater than for Ge (2.01) or Bi (2.02).[58]

Increasing the degree of $AgBiSe_2$ alloying thus increases the Ag content and, consequently, the ionic component of bonding. This can first of all explain the drive of the $(GeSe)_{1-x}-(AgBiSe_2)_x$ system toward a rock-salt cubic $Fm\bar{3}m$ arrangement with alloying: likely, an increasing ionic nature can favor higher-symmetry structures with less directional bonds.

Additionally, the DFT results provide insight into the sharp increase in stiffness observed due to the rhombohedral-to-cubic phase transition. Figure 5c,f shows the distribution of the A-Se (A = Ge, Ag, Bi) bond lengths present in each supercell. For the $R3m$ supercell (Figure 5c), the distribution of Ge−Se bond lengths is strongly bimodal, due to the lone pair expression of Ge $4s^2$ electrons, seen in the ELF maps. Ge therefore forms short covalent bonds with three neighboring Se atoms, and the lone pair is oriented to face the remaining three atoms (leading to 3 longer Ge−Se distances). Interestingly, some degree of bimodality is observed for the Ag−Se bonds, too, while the Bi−Se bonds seem unimodal. The Ge lone pair expression is observed in the rhombohedral and cubic structure (Figure 5a,b,d,e). However, in the rhombohedral structure only, the lone pairs are all oriented in the same direction, leading to extended 2D planes characterized by long Ge and Se distances. In the cubic arrangement, instead, Ge lone pairs are observed facing different directions. The latter is likely an expression of dynamical off-centering for the Ge cations, which overall leads to a disordered cubic arrangement when probed by statistical methods like standard XRD. Recent work on the related compound, GeTe, has argued that disorder in the cubic arrangement is a result of a dynamic motion of the Ge atoms rather than a static off-centering.[59] Dynamical off-centering has been proposed as being the origin of the soft, anharmonic lattices and low thermal conductivity in perovskites,[60,61] as well as in other rock-salt IV−VI compounds,[62] although the topic is controversial for the latter, with some authors attributing the effect to anharmonicity alone.[63] In the present material system, we can conclude that the switch from the directional lone-pair expression in the rhombohedral phase to the randomized/dynamic expression in the cubic phase is the origin of the large step-like increase in elastic moduli, with stiffer moduli being exhibited by the cubic phase.

In contrast to Ge, Ag does not form lone pairs, while the $6s^2$ lone pairs of Bi appear to be more symmetrically localized. This would point to the fact that the Ge lone pair is stereochemically expressed, thus occupying a distinct space around the cation and leading to a strong distortion, while the Bi lone pair is more stable in a symmetric dispersion around Bi. In general, lone pairs are expected to be more stable in heavier elements (i.e., lone-pair quenching).[61,64] It is interesting to notice that the ELF of the Bi lone pair loses some symmetry in the cubic arrangement, likely due to more repulsive

https://doi.org/10.1021/acs.chemmater.3c01616
Chem. Mater. XXXX, XXX, XXX−XXX

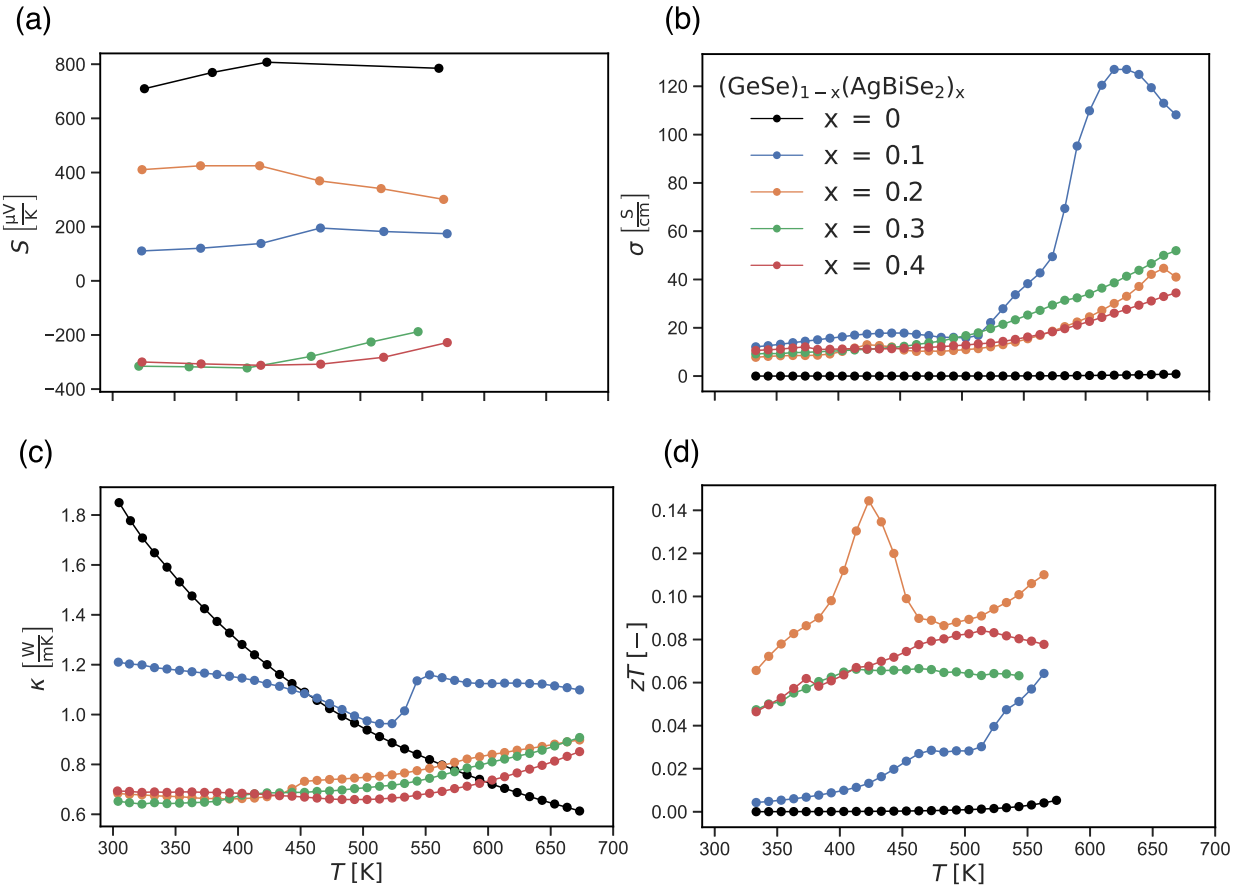

Figure 6. TE properties for the $(GeSe)_{1-x}$–$(AgBiSe_2)_x$ series, including (a) Seebeck coefficient S, (b) electrical conductivity σ, (c) thermal conductivity κ, and (d) figure of merit zT.

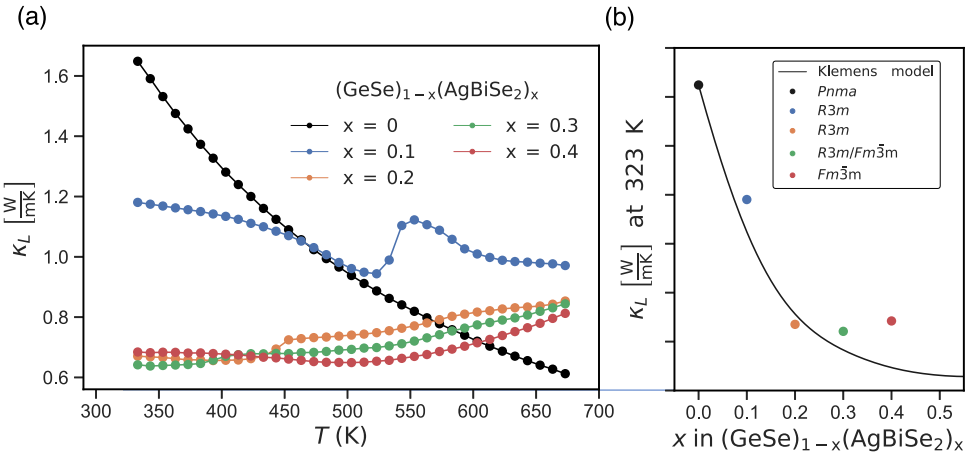

Figure 7. (a) Lattice thermal conductivity of $(GeSe)_{1-x}$–$(AgBiSe_2)_x$. Only GeSe shows a Umklapp-dominated κ_L. The alloying effect shows first a rapid κ_L suppression from $x = 0.1$ to $x = 0.2$, followed by smaller drop from $x = 0.2$ to $x = 0.3$. The $x = 0.4$ ($Fm\bar{3}m$) sample at room temperature breaks this trend, pointing to an intrinsically higher κ_L for the cubic polymorph. This is corroborated by the sharp increase in κ_L at the phase transition for the $x = 0.1$, 0.2, and 0.3 compounds. (b) Klemens model (black curve) for the lattice thermal conductivity κ_L of the $(GeSe)_{1-x}$–$(AgBiSe_2)_x$ system at room temperature, without taking into account the variation of the crystal structure with composition.

interactions with the randomly oriented, closer (due to the reduced unit-cell volume) Ge lone pairs (see additional ELF maps in Figure S6c and the Supporting Information). The bond length distribution of Ag and Bi (5c,f) is likely a byproduct of the Ge lone pairs straining the c-axis. Thus, as we add Ag and Bi, we increase the average bond length, thus softening the structure, as noticed in the decreasing trend of stiffness and κ_L, discussed later in the text, with alloying for the same crystal structure. Moreover, the Ag and Bi moderate the amount of bonding anisotropy in the rhombohedral structure, thus decreasing the disparity between the rhombohedral and cubic structures. This last feature is visible in the decreased rhombohedral-to-cubic stiffening as we increase the alloying fraction.

https://doi.org/10.1021/acs.chemmater.3c01616
Chem. Mater. XXXX, XXX, XXX−XXX

To directly probe the effect of crystal structure (without changing composition), we have performed DFT calculations on pure GeSe in the three different phases: orthorhombic *Pnma*, rhombohedral *R*3*m*, and cubic $Fm\bar{3}m$. Note that GeSe is orthorhombic, experimentally. The three calculations were performed with the same fixed volume in order to remove any possible influence of volume on the elastic moduli. The results—in Figure S7 in the Supporting Information—indicate that the cubic phase possesses higher elastic moduli and reduced anisotropy compared to the orthorhombic and rhombohedral phases. At the same time, if we compare the ELF going from the cubic to the rhombohedral structure (Figure S7c), we can see that the Ge lone pair expression trends from weaker to stronger. This further supports the connection between stronger lone pair expression, increased elastic anisotropy, and lower average elastic stiffness.

Transport Properties. We have observed that both alloying and structural arrangement play important roles in shaping the elastic behavior within the $(GeSe)_{1-x}-(AgBiSe_2)_x$ system. It is now interesting to explore the impact of these observed changes on the TE properties, specifically focusing on the thermal conductivity as it is intimately connected with elasticity. The TE transport properties are presented in Figure 6, including the Seebeck coefficient S, electrical conductivity σ, total thermal conductivity κ, and TE figure of merit zT. Note that the goal of this study was to study the thermal properties and not to optimize performance. Thus, as expected, all of the samples studied exhibit low zT values.

Pristine GeSe shows quite a high Seebeck coefficient and low electrical conductivity, indicative of an intrinsic semiconductor behavior, with values in accordance with other literature reports.[24,25] The alloyed samples show lower absolute S and higher σ, pointing to an increased carrier density. Interestingly, the electronic character passes from p- (x = 0.1 and 0.2 samples) to n-type (x = 0.3 and 0.4) with the progressive incorporation of $AgBiSe_2$. Cubic $(GeSe)_{1-x}-(AgBiSe_2)_x$ with x = 0.3−0.5 alloying has been reported in the literature to display n-type conduction.[25]

Lattice Thermal Conductivity. The lattice component of thermal conductivity, κ_L (Figure 7), was calculated as $\kappa_L = \kappa - \kappa_e$, where κ_e is the electronic component. This was estimated with the Wiedemann−Franz law as $\kappa_e = L\sigma T$, where L is the Lorenz number, calculated according to ref 65, and T is the absolute temperature. κ_e shows a negligible contribution for all the compositions (data in the Supporting Information, Figure S3). Above 450−500 K, the x = 0.2, 0.3, and 0.4 samples show an increasing trend of κ_L with temperature. This can be due to non-negligible bipolar effects. Thus, the plotted κ_L is likely a sum of the real κ_L and the bipolar contribution, κ_B. The bipolar effect is due to the thermal excitation and subsequent recombination of the carriers on the cold side of the sample. The presence of bipolar effects is also supported by the curved shaped of the Seebeck coefficient (Figure 6a). In the discussion below, we assume that below ∼500 K, the bipolar contribution is negligible, and κ_L is fully phononic in origin.

The κ_L of pristine GeSe shows a $T^{-1.4}$ behavior, indicative of thermal transport dominated by phonon−phonon scattering, or Umklapp, processes.[2,66,67] For compositions of x = 0.1, 0.2, and 0.3, the first evident feature is the step increase in κ_L (visible also in κ) at approximately 525, 425, and 380 K, respectively. This step-like increase is the direct result of the lattice stiffening (increased modulus) that occurs at the rhombohedral to cubic phase transition. The step in κ_L is much more pronounced for samples with less $AgBiSe_2$ content, consistent with the elastic behavior. For the three rhombohedral samples (x = 0.1, 0.2, and 0.3) below their phase transition temperatures, the progressive incorporation of Ag and Bi on the Ge site suppresses κ_L. The decay in the near room temperature κ_L is rapid from the x = 0.1 to x = 0.2 composition, followed by a much smaller drop from the x = 0.2 to the x = 0.3 sample. This suppression can be attributed in part to the decreased speed of sound with Ag and Bi alloying but must also be due to increased point defect scattering.

Indeed, the alloyed compositions exhibit generally flatter trends in κ_L than GeSe, pointing to additional phonon scattering sources, in particular, point defect scattering. Using the Klemens model for alloy scattering[4,68−71] (details in the Supporting Information), the expected effect of alloy scattering on the lattice thermal conductivity for the $(GeSe)_{1-x}-(AgBiSe_2)_x$ system was calculated and is displayed as the black curve in Figure 7b. Note that the Klemens model was developed for systems that form a complete solid solution with the same crystal structure throughout. Here, instead, we are dealing with three different structure types, each with different elastic constants and anharmonicities, leading to significant deviations from a simple Klemens model. It is evident that the current model (black line) underestimates the κ_L for the alloyed compositions in a cubic arrangement. This observation can be explained by the significant stiffening that occurs at the rhombohedral-to-cubic phase transition. At temperatures above the phase transition to the cubic arrangement, all the alloyed samples "recover" the trend of suppressed κ_L with increasing alloying, and the behavior predicted by the Klemens model is shown.

In order to decouple the effects of phonon velocity and phonon scattering on the behavior of κ_L, we turn to the simple model for κ_L based on the kinetic gas theory

$$\kappa_L = \frac{1}{3} C_v v^2 \tau \tag{2}$$

where C_v is the heat capacity at a constant volume, v is the phonon velocity, and τ is the phonon relaxation time. Here, we treat the phonon dispersion as Debye-like, assuming that the speed of sound is a reasonable ersatz for the frequency-dependent phonon group velocity. This simplification is useful for gaining insight into the trends in τ as a function of the composition, structure, and temperature. Thus, the scattering rate τ^{-1}, that is, the average number of phonon scattering events per unit time, was estimated using the measured κ_L and v_s and eq 2, where C_V was approximated by the Dulong−Petit limit. The results are shown in Figure 8, where the calculations were limited to the temperature range in which the bipolar contribution did not play a significant role. Additionally, discrepancies of the phase transition temperatures between the v_s and the κ_L measurements (likely due to instrumental differences in temperature measurement accuracy), as well as the intrinsic anomalous scattering rate around the phase transition, may give misleading τ^{-1} results. For this reason, the data points in the vicinity of the phase transition temperatures (labeled by hollow circles) are not considered in the following discussion.

The phonon scattering rate in this material is likely controlled by a combination of Umklapp, grain-boundary, and alloy or point-defect scattering.[72,73] The grain-boundary scattering rate is not expected to differ significantly among the samples, as Rietveld refinement estimates (see the Supporting

https://doi.org/10.1021/acs.chemmater.3c01616
Chem. Mater. XXXX, XXX, XXX−XXX

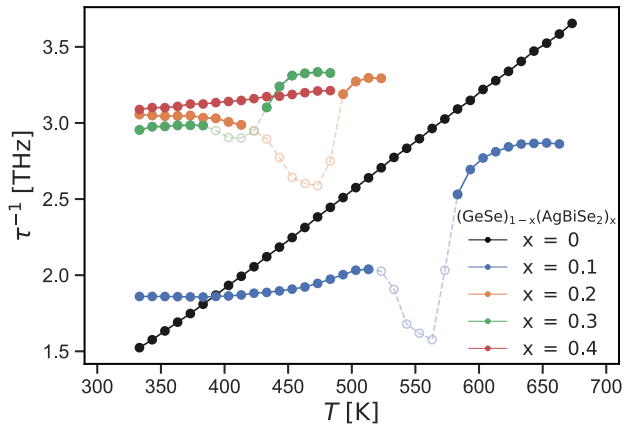

Figure 8. Calculated scattering rate τ^{-1} for the $(GeSe)_{1-x}$–$(AgBiSe_2)_x$ system. Hollow circles denote the τ^{-1} anomaly characteristic of the phase transition region. For the compositions of $x = 0.1$, 0.2, and 0.3, there is a clear increase in scattering rate after the rhombohedral-to-cubic phase transition.

Information) suggest a similar domain size throughout the compositions. From Figure 8, we can see that the scattering rate at room temperature increases with increasing $AgBiSe_2$ alloying. This is not surprising given the mass contrast and strain caused by the Ag and Bi on the Ge site. However, we also see that the scattering rate of the high-temperature cubic phase is substantially higher than that of the low-temperature rhombohedral phase. This suggests that there may be an inherent difference in the degree of Umklapp scattering between the two polymorphs. Umklapp processes are closely related to the anharmonic bonding features of a material, as quantified by the Grüneisen parameter. Although this is strictly mode dependent, thus rigorously obtained only via techniques like phonon DFT calculations or single-crystal neutron scattering experiments, it is possible to compute some thermodynamic estimates of the Grüneisen parameter via elasticity and thermal expansion data.[74] Calculations and details of the employed methods are reported in the Supporting Information. Although some difference in predictions among different methods are found—and in some degree expected[74]—we find that the estimates relying on thermal expansion show an increase in the Grüneisen parameter after the phase transition (i.e., the cubic phase may have greater overall anharmonicity). This may partly explain the observed increase in the phonon scattering rate in the cubic phase.

CONCLUSIONS

In conclusion, by using a combination of RUS, HT-XRD, and DFT, we investigated the influence of the crystal structure and composition on the lattice thermal conductivity of $(GeSe)_{1-x}$–$(AgBiSe_2)_x$ alloys. With an increase in the alloying, κ_L is progressively suppressed, but the trend is broken when different crystal structures are compared. In particular, samples with intermediate alloying fractions, facing a temperature-induced phase transformation from the rhombohedral to the cubic symmetry, present an increase in κ_L at the transition temperature. Interestingly, elasticity measurements show that this transition is accompanied by a marked lattice stiffening. The increase of alloying should be accompanied by a volume expansion due to the presence of the larger Ag and Bi atoms, and this is indeed observed when compositions within the same crystal structure are compared. However, the rhombohedral-to-cubic transformation results in a volume contraction that can partially explain the observed stiffening and higher κ_L. DFT provides further insights on this stiffening, suggesting a connection with the arrangement of Ge lone pairs. Indeed, these pass from being all oriented in the same direction in the rhombohedral symmetry, thus elongating certain bonds and softening the structure, to being randomly oriented in the cubic phase, leading to the observed lattice stiffening and increased κ_L with the transition. We expect that a similar stiffening occurs in any rock-salt chalcogenide exhibiting a rhombohedral-to-cubic transition, although it has not been widely recognized. The present study highlights the decoupled role of composition and structural features in elasticity, alloy scattering, and anharmonicity toward a fundamental understanding of thermal conductivity in this important class of TEs.

ASSOCIATED CONTENT

Supporting Information

The Supporting Information is available free of charge at https://pubs.acs.org/doi/10.1021/acs.chemmater.3c01616.

Rietveld refinement details; DSC and TGA; electronic characterization; alloy scattering calculations, including mass and radius variance estimations; and anharmonic contributions to phonon relaxation time (PDF)

AUTHOR INFORMATION

Corresponding Author

Alexandra Zevalkink − *Department of Chemical Engineering and Material Science, Michigan State University, East Lansing, Michigan 48824, United States;* orcid.org/0000-0002-4672-7438; Email: alexzev@msu.edu

Authors

Mario Calderón-Cueva − *Department of Chemical Engineering and Material Science, Michigan State University, East Lansing, Michigan 48824, United States;* orcid.org/0000-0001-7395-9747

Eleonora Isotta − *Department of Chemical Engineering and Material Science, Michigan State University, East Lansing, Michigan 48824, United States;* orcid.org/0000-0002-5864-463X

Megan Rylko − *Department of Chemical Engineering and Material Science, Michigan State University, East Lansing, Michigan 48824, United States;* orcid.org/0000-0002-3896-7706

Binayak Mukherjee − *Department of Civil, Environmental and Mechanical Engineering, University of Trento, Trento 38123, Italy;* Present Address: Luxembourg Institute of Science and Technology (LIST), Materials Research and Technology Department, Av. des Hauts-Fourneaux 5, Esch-sur-Alzette, L-4362, Luxembourg

Paolo Scardi − *Department of Civil, Environmental and Mechanical Engineering, University of Trento, Trento 38123, Italy;* orcid.org/0000-0003-1097-3917

Complete contact information is available at: https://pubs.acs.org/10.1021/acs.chemmater.3c01616

Notes

The authors declare no competing financial interest.

https://doi.org/10.1021/acs.chemmater.3c01616
Chem. Mater. XXXX, XXX, XXX−XXX

■ ACKNOWLEDGMENTS

The research was supported by the U.S. Department of Energy, Office of Basic Energy Sciences, Division of Materials Sciences and Engineering under the award DE-SC0019252.

■ REFERENCES

(1) Snyder, G. J.; Toberer, E. S. Complex thermoelectric materials. *Nat. Mater.* **2008**, *7*, 105−114.
(2) Toberer, E. S.; Zevalkink, A.; Snyder, G. J. Phonon engineering through crystal chemistry. *J. Mater. Chem.* **2011**, *21*, 15843−15852.
(3) Walker, C.; Pohl, R. Phonon scattering by point defects. *Phys. Rev.* **1963**, *131*, 1433−1442.
(4) Klemens, P. The scattering of low-frequency lattice waves by static imperfections. *Proc. Phys. Soc., London, Sect. A* **1955**, *68*, 1113−1128.
(5) Ohashi, K.; Ohashi, Y. Mean-square displacement of a vibrating dislocation. *Philos. Mag. A* **1978**, *38*, 187−204.
(6) Egorov, S.; Skinner, J. On the theory of multiphonon relaxation rates in solids. *J. Chem. Phys.* **1995**, *103*, 1533−1543.
(7) Wang, J.-S.; Wang, J.; Lü, J. T. Quantum thermal transport in nanostructures. *Eur. Phys. J. B* **2008**, *62*, 381−404.
(8) Vineis, C. J.; Shakouri, A.; Majumdar, A.; Kanatzidis, M. G. Nanostructured thermoelectrics: big efficiency gains from small features. *Adv. Mater.* **2010**, *22*, 3970−3980.
(9) Rowe, D.; Shukla, V.; Savvides, N. Phonon scattering at grain boundaries in heavily doped fine-grained silicon−germanium alloys. *Nature* **1981**, *290*, 765−766.
(10) Shevelkov, A. V. Chemical aspects of the design of thermoelectric materials. *Russ. Chem. Rev.* **2008**, *77*, 1−19.
(11) Toberer, E. S.; May, A. F.; Snyder, G. J. Zintl chemistry for designing high efficiency thermoelectric materials. *Chem. Mater.* **2010**, *22*, 624−634.
(12) Wu, D.; Zhao, L.-D.; Tong, X.; Li, W.; Wu, L.; Tan, Q.; Pei, Y.; Huang, L.; Li, J.-F.; Zhu, Y.; et al. Superior thermoelectric performance in PbTe−PbS pseudo-binary: extremely low thermal conductivity and modulated carrier concentration. *Energy Environ. Sci.* **2015**, *8*, 2056−2068.
(13) Lee, M. H.; Yun, J. H.; Kim, G.; Lee, J. E.; Park, S.-D.; Reith, H.; Schierning, G.; Nielsch, K.; Ko, W.; Li, A.-P.; et al. others Synergetic enhancement of thermoelectric performance by selective charge Anderson localization−delocalization transition in n-type Bi-doped PbTe/Ag_2Te nanocomposite. *ACS Nano* **2019**, *13*, 3806−3815.
(14) Liu, H.-T.; Sun, Q.; Zhong, Y.; Deng, Q.; Gan, L.; Lv, F.-L.; Shi, X.-L.; Chen, Z.-G.; Ang, R. High-performance in n-type PbTe-based thermoelectric materials achieved by synergistically dynamic doping and energy filtering. *Nano Energy* **2022**, *91*, 106706.
(15) Komisarchik, G.; Gelbstein, Y.; Fuks, D. Solubility of Ti in thermoelectric PbTe compound. *Intermetallics* **2017**, *89*, 16−21.
(16) Li, J.; Zhang, X.; Chen, Z.; Lin, S.; Li, W.; Shen, J.; Witting, I. T.; Faghaninia, A.; Chen, Y.; Jain, A.; et al. Low-Symmetry Rhombohedral GeTe Thermoelectrics. *Joule* **2018**, *2*, 976−987.
(17) Tsai, Y.-F.; Wei, P.-C.; Chang, L.; Wang, K.-K.; Yang, C.-C.; Lai, Y.-C.; Hsing, C.-R.; Wei, C.-M.; He, J.; Snyder, G. J. Thermoelectric Materials: Compositional Fluctuations Locked by Athermal Transformation Yielding High Thermoelectric Performance in GeTe (Adv. Mater. 1/2021). *Adv. Mater.* **2021**, *33*, 2170008.
(18) Jiang, B.; Wang, W.; Liu, S.; Wang, Y.; Wang, C.; Chen, Y.; Xie, L.; Huang, M.; He, J. High figure-of-merit and power generation in high-entropy GeTe-based thermoelectrics. *Science* **2022**, *377*, 208−213.
(19) Dado, B.; Gelbstein, Y.; Dariel, M. P. Nucleation of nanosize particles following the spinodal decomposition in the pseudo-ternary $Ge_{0.6}Sn_{0.1}Pb_{0.3}Te$ compound. *Scr. Mater.* **2010**, *62*, 89−92.
(20) Zhao, L.-D.; Lo, S.-H.; Zhang, Y.; Sun, H.; Tan, G.; Uher, C.; Wolverton, C.; Dravid, V. P.; Kanatzidis, M. G. Ultralow thermal conductivity and high thermoelectric figure of merit in SnSe crystals. *Nature* **2014**, *508*, 373−377.
(21) Chang, C.; Wu, M.; He, D.; Pei, Y.; Wu, C.-F.; Wu, X.; Yu, H.; Zhu, F.; Wang, K.; Chen, Y.; et al. 3D charge and 2D phonon transports leading to high out-of-plane *ZT* in n-type SnSe crystals. *Science* **2018**, *360*, 778−783.
(22) Zhou, C.; Lee, Y. K.; Yu, Y.; Byun, S.; Luo, Z.-Z.; Lee, H.; Ge, B.; Lee, Y.-L.; Chen, X.; Lee, J. Y.; et al. Polycrystalline SnSe with a thermoelectric figure of merit greater than the single crystal. *Nat. Mater.* **2021**, *20*, 1378−1384.
(23) Hao, S.; Shi, F.; Dravid, V. P.; Kanatzidis, M. G.; Wolverton, C. Computational prediction of high thermoelectric performance in hole doped layered GeSe. *Chem. Mater.* **2016**, *28*, 3218−3226.
(24) Zhang, X.; Shen, J.; Lin, S.; Li, J.; Chen, Z.; Li, W.; Pei, Y. Thermoelectric properties of GeSe. *J. Materi.* **2016**, *2*, 331−337.
(25) Roychowdhury, S.; Ghosh, T.; Arora, R.; Waghmare, U. V.; Biswas, K. Stabilizing n-Type Cubic GeSe by Entropy-Driven Alloying of $AgBiSe_2$: Ultralow Thermal Conductivity and Promising Thermoelectric Performance. *Angew. Chem., Int. Ed.* **2018**, *57*, 15167.
(26) Shaabani, L.; Aminorroaya-Yamini, S.; Byrnes, J.; Akbar Nezhad, A.; Blake, G. R. Thermoelectric performance of Na-doped GeSe. *ACS Omega* **2017**, *2*, 9192−9198.
(27) Böcher, F.; Culver, S. P.; Peilstöcker, J.; Weldert, K. S.; Zeier, W. G. Vacancy and anti-site disorder scattering in $AgBiSe_2$ thermoelectrics. *Dalton Trans.* **2017**, *46*, 3906−3914.
(28) Sarkar, D.; Ghosh, T.; Roychowdhury, S.; Arora, R.; Sajan, S.; Sheet, G.; Waghmare, U. V.; Biswas, K. Ferroelectric instability induced ultralow thermal conductivity and high thermoelectric performance in rhombohedral p-type GeSe crystal. *J. Am. Chem. Soc.* **2020**, *142*, 12237−12244.
(29) Tippireddy, S.; Azough, F.; Bhui, A.; Bhui, A.; Chater, P.; Kepaptsoglou, D.; Ramasse, Q.; Freer, R.; Grau-Crespo, R.; Biswas, K.; et al. Local structural distortions and reduced thermal conductivity in Ge-substituted chalcopyrite. *J. Mater. Chem. A* **2022**, *10*, 23874−23885.
(30) Kolobov, A. V.; Fons, P.; Tominaga, J. p-Type conductivity of GeTe: The role of lone-pair electrons. *Phys. Status Solidi B* **2012**, *249*, 1902−1906.
(31) Waghmare, U.; Spaldin, N.; Kandpal, H. C.; Seshadri, R. First-principles indicators of metallicity and cation off-centricity in the IV-VI rocksalt chalcogenides of divalent Ge, Sn, and Pb. *Phys. Rev. B: Condens. Matter Mater. Phys.* **2003**, *67*, 125111.
(32) Raty, J.-Y.; Wuttig, M. The interplay between Peierls distortions and metavalent bonding in IV−VI compounds: comparing GeTe with related monochalcogenides. *J. Phys. D: Appl. Phys.* **2020**, *53*, 234002.
(33) de Boer, T.; Somers, C.; Boyko, T.; Ambach, S.; Eisenburger, L.; Schnick, W.; Moewes, A. The importance of lone pairs to structure and bonding of the novel germanium nitridophosphate GeP_2N_4. *J. Mater. Chem. A* **2023**, *11*, 6198−6204.
(34) Wiedemeier, H.; Siemers, P. The thermal expansion and high temperature transformation of GeSe. *Z. Anorg. Allg. Chem.* **1975**, *411*, 90−96.
(35) Coelho, A. A. TOPAS and TOPAS-Academic: An optimization program integrating computer algebra and crystallographic objects written in C++ J. *Appl. Crystallogr.* **2018**, *51*, 210−218.
(36) Scardi, P.; Azanza Ricardo, C. L.; Perez-Demydenko, C.; Coelho, A. A. Whole powder pattern modelling macros for TOPAS. *J. Appl. Crystallogr.* **2018**, *51*, 1752−1765.
(37) Scardi, P. *Powder Diffraction: Theory and Practice*; Dinnebier, R. E., Billinge, S., Eds.; Royal Society of Chemistry: Cambridge, 2008; Chapter 13; pp 378−417.
(38) Balakirev, F. F.; Ennaceur, S. M.; Migliori, R. J.; Maiorov, B.; Migliori, A. Resonant ultrasound spectroscopy: The essential toolbox. *Rev. Sci. Instrum.* **2019**, *90*, 121401.
(39) Migliori, A.; Sarrao, J.; Visscher, W. M.; Bell, T.; Lei, M.; Fisk, Z.; Leisure, R. G. Resonant ultrasound spectroscopic techniques for measurement of the elastic moduli of solids. *Phys. B* **1993**, *183*, 1−24.
(40) Borup, K. A.; De Boor, J.; Wang, H.; Drymiotis, F.; Gascoin, F.; Shi, X.; Chen, L.; Fedorov, M. I.; Müller, E.; Iversen, B. B.; et al. Measuring thermoelectric transport properties of materials. *Energy Environ. Sci.* **2015**, *8*, 423−435.

https://doi.org/10.1021/acs.chemmater.3c01616
Chem. Mater. XXXX, XXX, XXX−XXX

(41) Kresse, G.; Furthmüller, J. Efficient iterative schemes for ab initio total-energy calculations using a plane-wave basis set. *Phys. Rev. B: Condens. Matter Mater. Phys.* **1996**, *54*, 11169−11186.
(42) Kresse, G.; Furthmüller, J. Efficiency of ab-initio total energy calculations for metals and semiconductors using a plane-wave basis set. *Comput. Mater. Sci.* **1996**, *6*, 15−50.
(43) Perdew, J. P.; Burke, K.; Ernzerhof, M. Generalized gradient approximation made simple. *Phys. Rev. Lett.* **1996**, *77*, 3865−3868.
(44) Perdew, J. P.; Ruzsinszky, A.; Csonka, G. I.; Vydrov, O. A.; Scuseria, G. E.; Constantin, L. A.; Zhou, X.; Burke, K. Restoring the density-gradient expansion for exchange in solids and surfaces. *Phys. Rev. Lett.* **2008**, *100*, 136406.
(45) Momma, K.; Izumi, F. VESTA 3 for three-dimensional visualization of crystal, volumetric and morphology data. *J. Appl. Crystallogr.* **2011**, *44*, 1272−1276.
(46) Dutta, S.; Jeffrey, G. On the structure of germanium selenide and related binary IV/VI compounds. *Inorg. Chem.* **1965**, *4*, 1363−1366.
(47) Kannewurf, C.; Kelly, A.; Cashman, R. Comparison of three structure determinations for germanium selenide, GeSe. *Acta Crystallogr.* **1960**, *13*, 449−450.
(48) Okazaki, A. The crystal structure of germanium selenide GeSe. *J. Phys. Soc. Jpn.* **1958**, *13*, 1151−1155.
(49) Abrikosov, N. K. *Semiconducting II−VI, IV−VI, and V−VI Compounds*; Springer, 2013; Chapter 2, pp 65−103.
(50) Huang, Z.; Miller, S. A.; Ge, B.; Yan, M.; Anand, S.; Wu, T.; Nan, P.; Zhu, Y.; Zhuang, W.; Snyder, G. J.; et al. High thermoelectric performance of new rhombohedral phase of GeSe stabilized through alloying with $AgSbSe_2$. *Angew. Chem., Int. Ed.* **2017**, *56*, 14113.
(51) Guin, S. N.; Srihari, V.; Biswas, K. Promising thermoelectric performance in n-type $AgBiSe_2$: effect of aliovalent anion doping. *J. Mater. Chem. A* **2015**, *3*, 648−655.
(52) Aliev, I.; Babanly, K.; Babanly, N. Solid solutions in the Ag_2Se-PbSe-Bi_2Se_3 system. *Inorg. Mater.* **2008**, *44*, 1179−1182.
(53) Iizumi, M.; Hamaguchi, Y.; F Komatsubara, K.; Kato, Y. Phase transition in SnTe with low carrier concentration. *J. Phys. Soc. Jpn.* **1975**, *38*, 443−449.
(54) Chatterji, T.; Kumar, C.; Wdowik, U. D. Anomalous temperature-induced volume contraction in GeTe. *Phys. Rev. B: Condens. Matter Mater. Phys.* **2015**, *91*, 054110.
(55) Bierly, J.; Muldawer, L.; Beckman, O. The continuous rhombohedral-gubic transformation in GeTe-SnTe alloys. *Acta Metall.* **1963**, *11*, 447−454.
(56) Shimada, T.; Kobayashi, K. L.; Katayama, Y.; Komatsubara, K. Soft-phonon-induced Raman scattering in IV-VI compounds. *Phys. Rev. Lett.* **1977**, *39*, 143−146.
(57) Silvi, B.; Savin, A. Classification of chemical bonds based on topological analysis of electron localization functions. *Nature* **1994**, *371*, 683−686.
(58) Pauling, L. *The Chemical Bond: A Brief Introduction to Modern Structural Chemistry*; Cornell University Press, 1967; Chapter 3, pp 49−69.
(59) Kimber, S. A. J.; Zhang, J.; Liang, C. H.; Guzmán-Verri, G. G.; Littlewood, P. B.; Cheng, Y.; Abernathy, D. L.; Hudspeth, J. M.; Luo, Z.-Z.; Kanatzidis, M. G. Dynamic crystallography reveals spontaneous anisotropy in cubic GeTe. *Nat. Mater.* **2023**, *22*, 311.
(60) Xie, H.; Hao, S.; Bao, J.; Slade, T. J.; Snyder, G. J.; Wolverton, C.; Kanatzidis, M. G. All-inorganic halide perovskites as potential thermoelectric materials: dynamic cation off-centering induces ultralow thermal conductivity. *J. Am. Chem. Soc.* **2020**, *142*, 9553−9563.
(61) Laurita, G.; Fabini, D. H.; Stoumpos, C. C.; Kanatzidis, M. G.; Seshadri, R. Chemical tuning of dynamic cation off-centering in the cubic phases of hybrid tin and lead halide perovskites. *Chem. Sci.* **2017**, *8*, 5628−5635.
(62) Holm, K. A. U.; Roth, N.; Zeuthen, C. M.; Iversen, B. B. Anharmonicity and correlated dynamics of PbTe and PbS studied by single crystal x-ray scattering. *Phys. Rev. B* **2021**, *103*, 224302−224307.
(63) Li, C. W.; Ma, J.; Cao, H. B.; May, A. F.; Abernathy, D. L.; Ehlers, G.; Hoffmann, C.; Wang, X.; Hong, T.; Huq, A.; Gourdon, O.; Delaire, O. Anharmonicity and atomic distribution of SnTe and PbTe thermoelectrics. *Phys. Rev. B: Condens. Matter Mater. Phys.* **2014**, *90*, 214303−214310.
(64) Zeier, W. G.; Zevalkink, A.; Gibbs, Z. M.; Hautier, G.; Kanatzidis, M. G.; Snyder, G. J. Thinking like a chemist: intuition in thermoelectric materials. *Angew. Chem., Int. Ed.* **2016**, *55*, 6826−6841.
(65) Kim, H.-S.; Gibbs, Z. M.; Tang, Y.; Wang, H.; Snyder, G. J. Characterization of Lorenz number with Seebeck coefficient measurement. *APL Mater.* **2015**, *3*, 041506.
(66) Klemens, P. G. *Thermal Conductivity*; Tye, R. P., Ed.; Academic Press: London, 1969; Vol. *1−68*, Chapter 1.
(67) Roufosse, M.; Klemens, P. Thermal conductivity of complex dielectric crystals. *Phys. Rev. B: Solid State* **1973**, *7*, 5379−5386.
(68) Callaway, J.; von Baeyer, H. C. Effect of point imperfections on lattice thermal conductivity. *Phys. Rev.* **1960**, *120*, 1149−1154.
(69) Klemens, P. Thermal resistance due to point defects at high temperatures. *Phys. Rev.* **1960**, *119*, 507−509.
(70) Goldsmid, H. Recent studies of bismuth telluride and its alloys. *J. Appl. Phys.* **1961**, *32*, 2198−2202.
(71) Gurunathan, R.; Hanus, R.; Snyder, G. J. Alloy scattering of phonons. *Mater. Horiz.* **2020**, *7*, 1452−1456.
(72) Matthiessen, A.; Vogt, C. Ueber den Einfluss der Temperatur auf die elektrische Leitungsfahigkeit der Legirungen. *Ann. Phys.* **1864**, *198*, 19−78.
(73) Ziman, J. *Electrons and Phonons: The Theory of Transport Phenomena in Solids*; Oxford University Press, 2001.
(74) Isotta, E.; Peng, W.; Balodhi, A.; Zevalkink, A. Elastic moduli: a tool for understanding chemical bonding and thermal transport in thermoelectric materials. *Angew. Chem., Int. Ed.* **2023**, *62*, No. e202213649.

https://doi.org/10.1021/acs.chemmater.3c01616
Chem. Mater. XXXX, XXX, XXX−XXX